Supporting Information for:

Filling carbon: a microstructure-engineered hard carbon for efficient alkali metal-ion storage

Experimental methods

Chemical vapor deposition (CVD). The activated carbon (AC) (YEC-8A) and purchased mesoporous carbon CMK-3 were used as templates without further modification. Typically, a certain of AC was spread evenly over the bottom of the Al_2O_3 boat. Then the boat was placed inside a tube furnace and heated to 700 ^oC with a heating ramp rate of 10 ^oC min^{-1} under Ar condition as the gas carrier in a flow rate of 100 SCCM. And then CVD step was carried out at 700 ^oC for various residence time of 0, 40 min, 1 h, and 3 h while introducing a certain flow rate of benzene vapor. The as-obtained products were denoted as AC, FC-40min, FC-1h, and FC-3h, respectively. In addition, CMK-3 was also been used as templets with the same procedure while the residence time was prolonged to 0, 6, 9, and 12 h, and the as-obtained samples were denoted as CMK-3, CMK-3-6h, CMK-3-9h, and CMK-3-12h, respectively. To investigate the influence of carbon sources, benzene was replaced by ethyne, methyl ethyl sulfide, toluene, thiophene, and pyridine, and the other conditions remain unchanged.

Post-heat treatment. To further adjust the microstructures of the filling carbon (FC) samples, FC-3h was further post-heat treated at 1100, 1300, and 1500 ^oC for 2 h under an Ar atmosphere with a ramp rate of 1 ^oC min^{-1}. The obtained carbon materials were denoted as FC-3h-1100, FC-3h-1300, and FC-3h-1500, respectively. To exclude the influence of post-heat treatment on the template, AC was also heat treated at 1300 ^oC

for 2 h and denoted as AC-1300.

Materials characterization. The morphologies of samples were observed by scanning electron microscopy (SEM) (ULTRA/PLUS, ZEISS) and high-resolution transmission electron microscopy (HRTEM) (FEI TF20). The crystal phases were analyzed by X-ray diffraction (XRD) (Rigaku SmartLab SE; Rigaku) with Cu Kα radiation (λ = 0.15406 nm) and Raman spectroscopies (DXR2; Thermo Fisher Scientific) with a laser wavelength of 532 nm. The porous textures were characterized by adsorption-desorption measurements (iPore 400), true density analysis (iPYC10), and the small angle X-ray scattering (SAXS) technique. The N_2 and CO_2 adsorption-desorption isotherm were respectively obtained at 77 K and 273 K and analyzed by the density functional theory (DFT) method to obtain the open pore size distribution. The specific surface area was calculated based on the N_2 adsorption isotherm by using the Brunauer–Emmett–Teller (BET) method. The true density was measured by using the He replacement method due to the ultra-small aerodynamic diameter of the He molecule to derive the closed pore volume. The SAXS profiles were collected on a Rigaku 3.5 m NANOPIX system equipped with a Cu kα radiation source using the transmission method. The data were fitted by using a Nano Solver software assuming a cylinder model to obtain the average pore diameter.

Electrochemical Measurement. The electrochemical performances of carbon materials were examined using CR2032-coin cells assembled in an argon-filled glove box. Na, K, or Li foil and glass fiber (GF/F, whatman) were used as counter electrodes and separators for sodium, potassium, and lithium batteries, respectively. The electrolyte was 1 M $NaPF_6$ in diethylene glycol dimethyl for Na half-cells, 1M $LiPF_6$ in ethylene carbonate/ethyl methyl carbonate /dimethyl carbonate (1:1:1 by volume) for Li half-cells, and 1 M KPF_6 in ethylene carbonate/diethyl carbonate (1:1 by volume) K half-cells. The working electrodes were prepared by mixing active materials, polyacrylic acid (PAA), and Super P (8:1:1 by weight) in deionized water to form a homogenous slurry. The slurry was spread on a Cu foil and dried at 100 ^oC for 12 h under vacuum and then punched into small disks with a diameter of 12 mm and mass

loading of ~ 1.5 mg cm^{-2}. Sodium and potassium storage performance was examined in a galvanostatic charge-discharge mode in the potential range of 0.002-3 V at a current density of 20 mA g^{-1} using a battery test system. The lithium storage performance was tested in the constant-current/constant-potential (CC/CP) mode at a current density of 20 mA g^{-1} with a cutoff voltage of 0.005 V and then discharged to 4 mA g^{-1}. The slow scan rate cycling voltammetry (CV) measurements were carried out in the potential range of 0.002-1.5 V versus Na/Na^+ at a scan rate of 0.01 mV s^{-1} using an IviumNstat electrochemical workstation.

Operando Analysis. The work electrodes were composed of 90 wt.% active materials and 10 wt.% polytetrafluoroethylene (PTFE) without any conductive carbon. Operando analysis was performed in a special in-situ cell with a beryllium window for XRD analysis and a quartz plate for Raman analysis as an optical window. The in-situ cells were tested in the potential range of 0.002-2 V at a constant current density of 20 mA g^{-1} for XRD analysis and 50 mA g^{-1} for Raman analysis.

Computational details. All calculations were implemented in the framework of the spin-polarized density functional theory (DFT) with generalized gradient approximation (GGA)[1] and Perdew-Burke-Ernzerhof (PBE)[2] exchange functional. Vienna Abinitio Simulation Package (VASP)[3, 4] with the projector augment wave (PAW)[5] method was employed in DFT calculations. For structure optimization, the cutoff energy of plane-wave basis set and Monkhorst-Pack k-points meshes were set as 450 eV and 2 × 2 × 1. In addition, the self-consistent convergence accuracy was set as 1×10^{-6} eV/atom, while the convergence criterion for the force between atoms was 1×10^{-2} eV/Å.

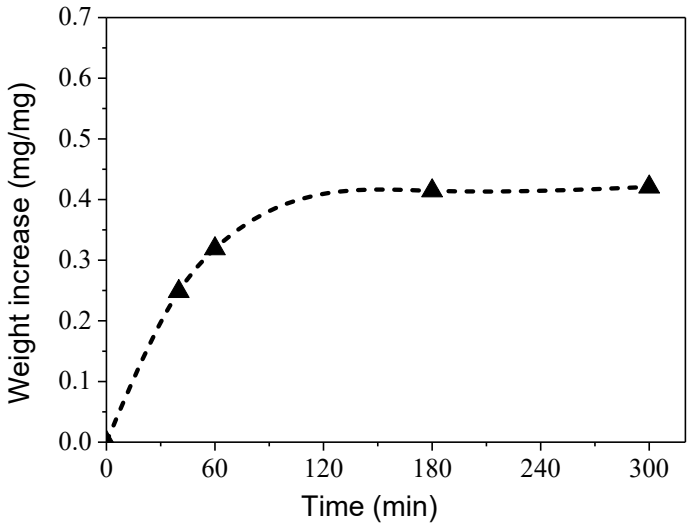

Fig. S1 The weight increase of AC during the CVD treatment.

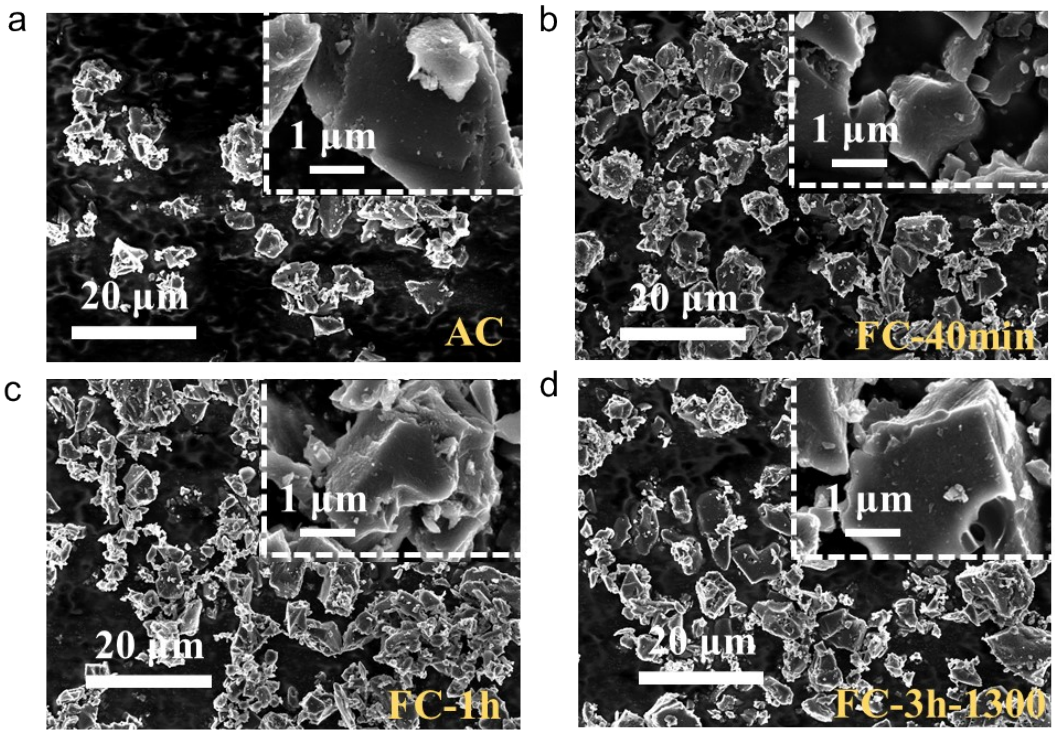

Fig. S2 The SEM images of FC samples. SEM images of (a) AC, (b) FC-40min, (c) FC-1h, and (d) FC-3h-1300 samples.

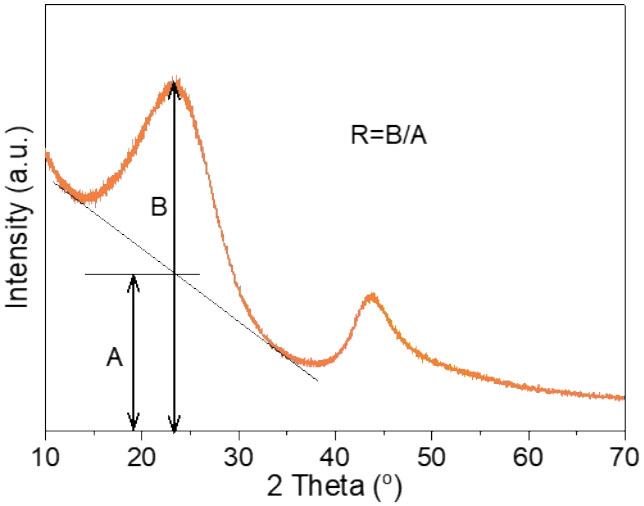

Fig. S3 Schematic representation of the definition of the parameter R used to empirically estimate the fraction of single-layers in hard carbon samples.

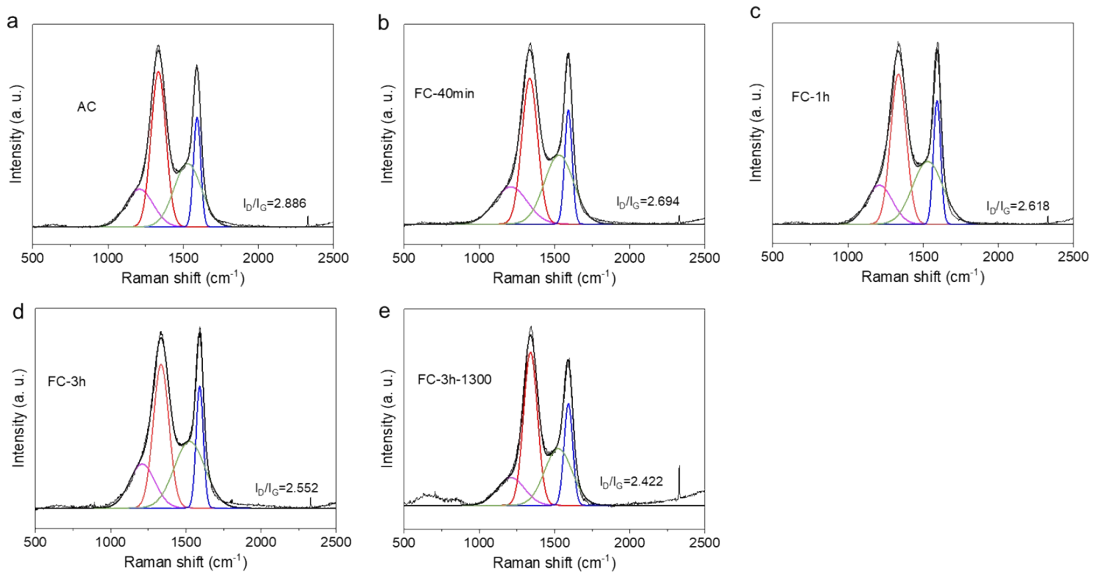

Fig. S4 The fitting results of Raman spectra of FC samples. The fitting results of Raman spectra of (a) AC, (b) FC-40min, (c) FC-1h, (d) FC-3h, and (e) FC-3h-1300 samples.

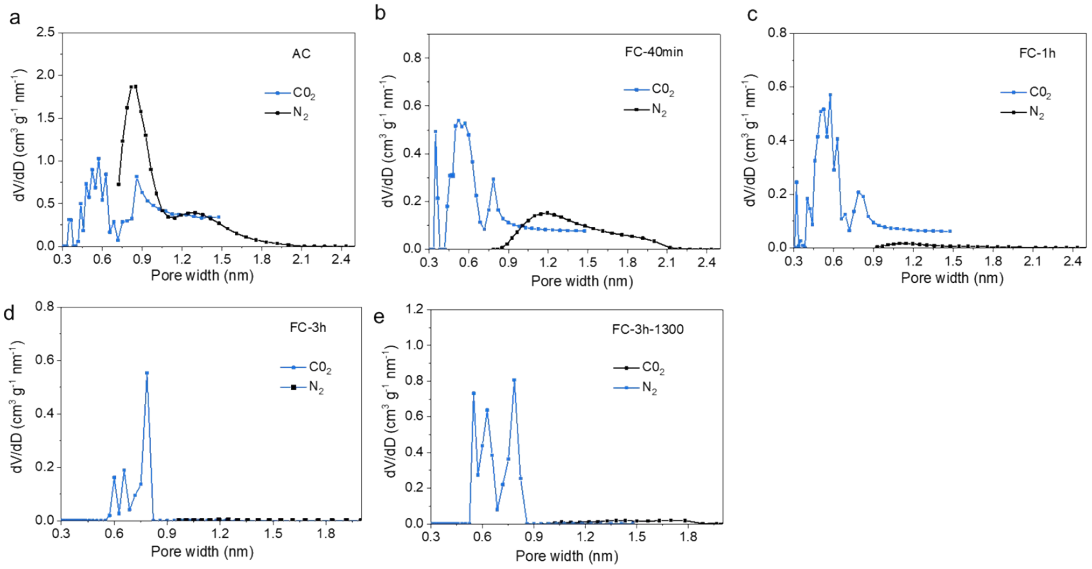

Fig. S5 The open pore size distributions of FC samples. The pore size distributions of (a) AC, (b) FC-40min, (c) FC-1h, (d) FC-3h, and (e) FC-3h-1300 samples obtained by fitting the N_2 and CO_2 adsorption isotherms.

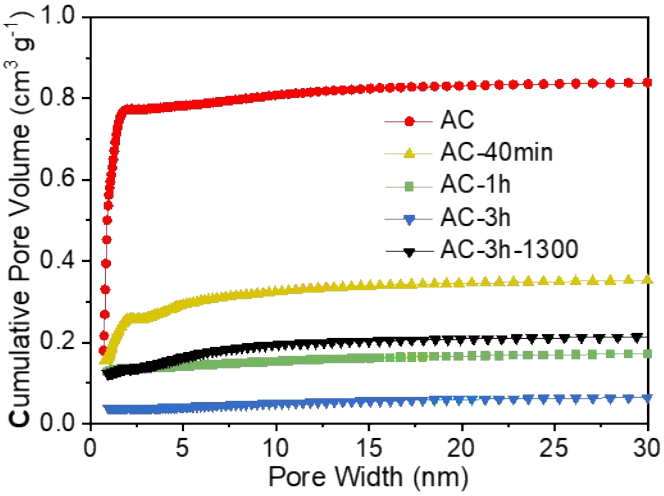

Fig. S6 The cumulative diagram of pore size distribution.

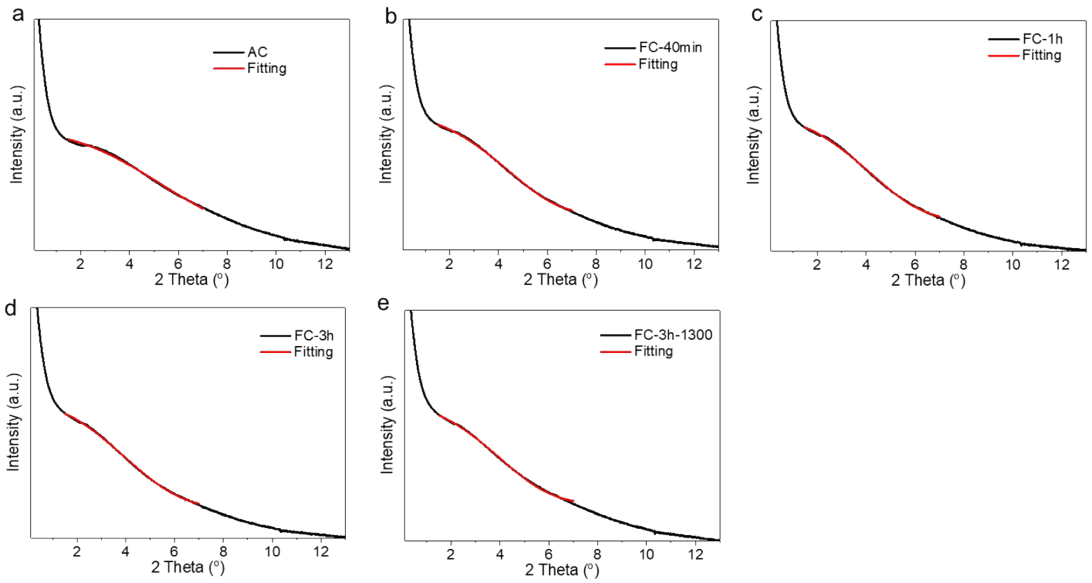

Fig. S7 The fitting results of SAXS patterns of FC samples. The fitting results of SAXS patterns of (a) AC, (b) FC-40min, (c) FC-1h, (d) FC-3h, and (e) FC-3h-1300 samples.

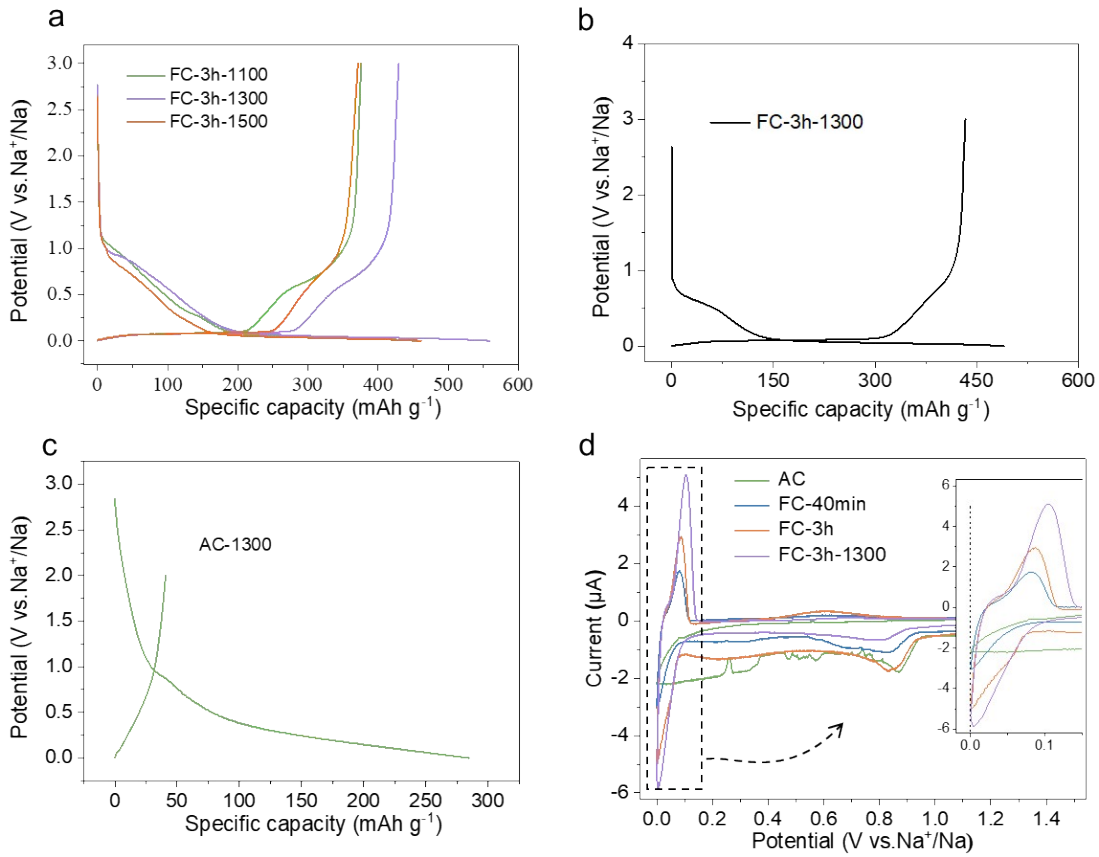

Fig. S8 Sodium ions storage behaviors of FC electrodes. (a) The initial discharge-charge profiles of FC-3h-1100, FC-3h-1300, and FC-3h-1500 electrodes at a current density of 20 mA g^{-1}. (b) The initial discharge-charge profiles of FC-3h-1300 without conductive carbon black at a current density of 20 mA g^{-1}. The FC-3h-1300 electrode was prepared with active material and polyacrylic acid (PAA) (9:1 by weight) to exclude the influence of Super P on the ICE. (c) The initial discharge-charge profiles of AC-1300 electrode at a current density of 20 mA g^{-1}. (d) The initial CV profiles of the AC and FC samples at a slow scan rate of 0.01 mV s^{-1}.

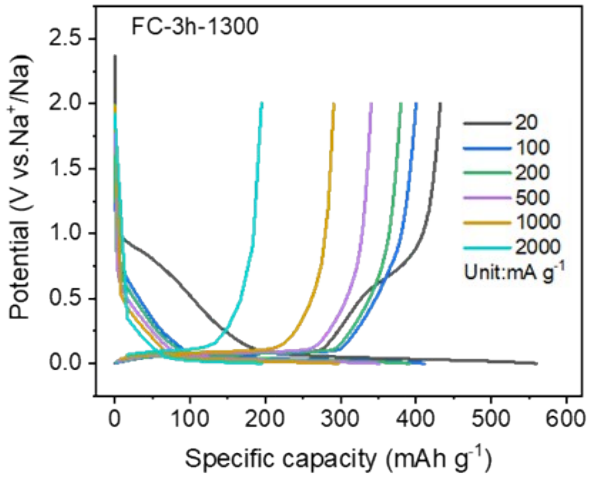

Fig. S9 The discharge/charge curves of the FC-3h-1300 electrode for sodium-ion batteries at different current densities.

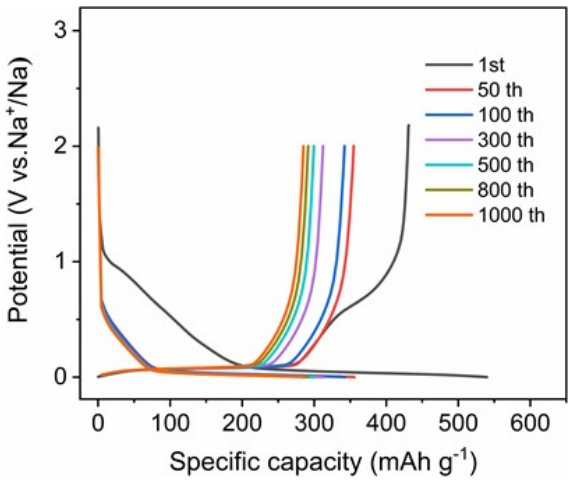

Fig. S10 The discharge/charge curves of the FC-3h-1300 electrode at different cycles for sodium-ion batteries.

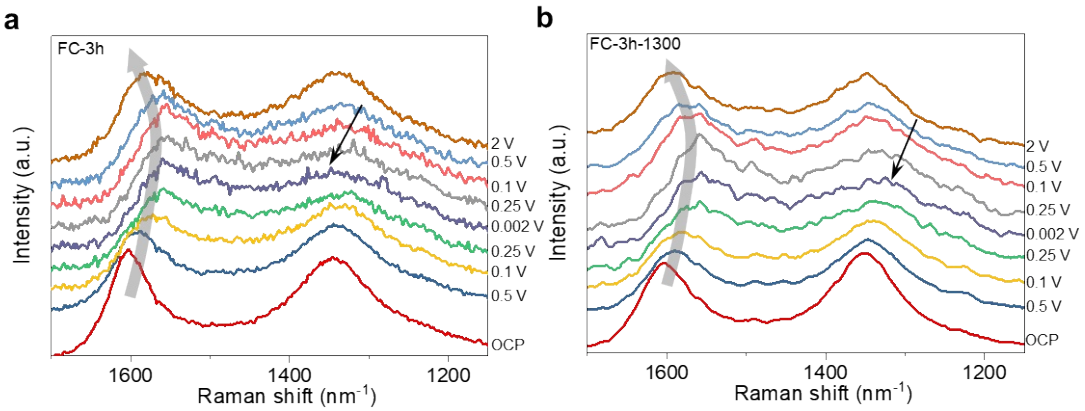

Fig. S11 In situ Raman studies of the FC electrodes. Evolution of Raman spectra of (a) FC-3h and (b) FC-3h-1300 electrodes collected in operando mode at different discharge and charge states.

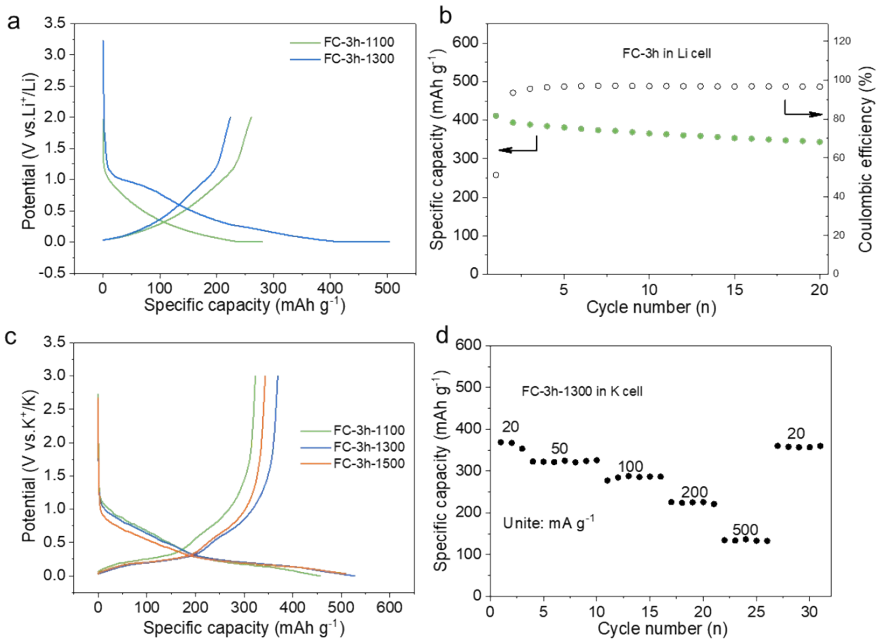

Fig. S12 Lithium and potassium ion storage behaviors of FC electrodes. (a) The initial charge-discharge curves of FC-3h-1100 and FC-3h-1300 electrodes in Li half-cells at a current density of 20 mA g^{-1} with a cutoff voltage of 0.005 V and then discharged at 0.005 V to 4 mA g^{-1}. (b) The cycling performance of FC-3h electrode in CC/CV mode in Li half-cells. (c) The initial discharge-charge profiles of FC-3h-1100, FC-3h-1300, and FC-3h-1500 electrodes at a current density of 20 mA g^{-1} in K half-cells. (d) The rate performance of FC-3h-1300 electrodes at various current densities in K half-cells.

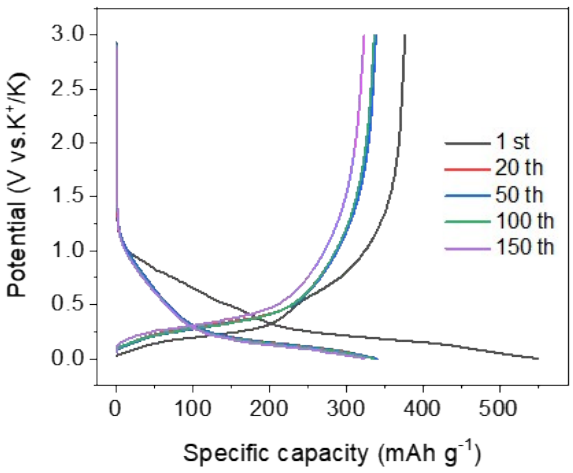

Fig. S13 The discharge-charge curve of FC-3h-1300 electrode at different cycles for potassium-ion batteries.

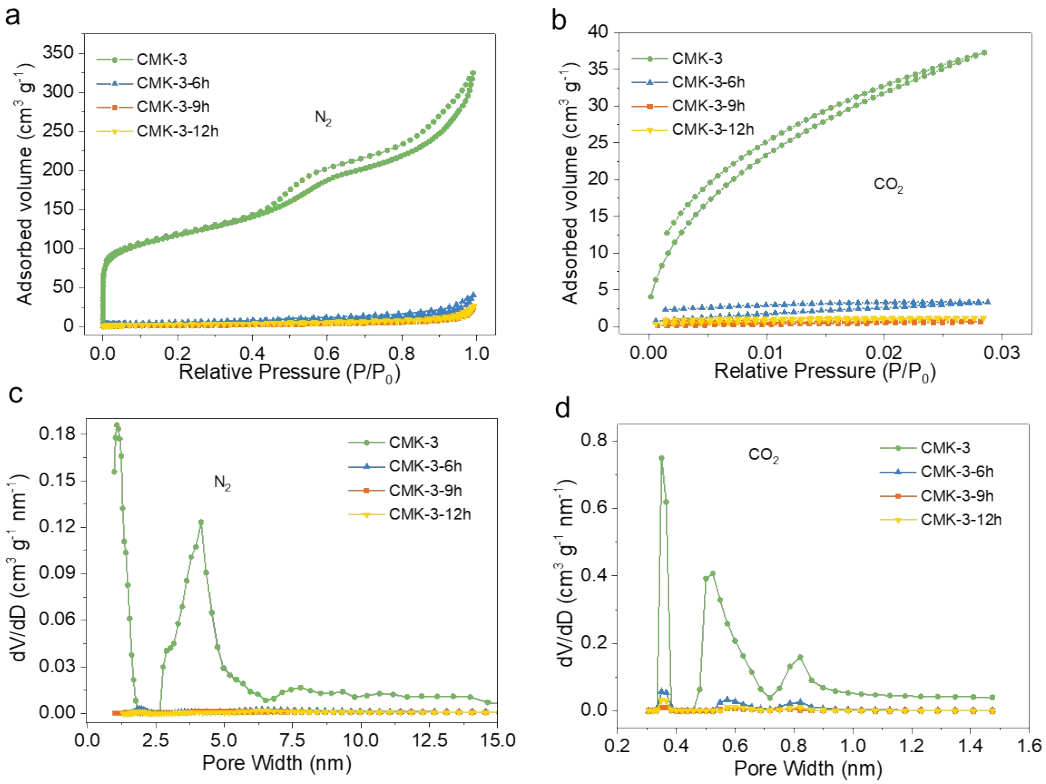

Fig. S14 The open pore structures of the CMK-3 and CVD-treated CMK-3. The (a) N_2 and (b) CO_2 adsorption-desorption isotherms and (c), (d) the corresponding pore size distributions of CVD-treated CMK-3.

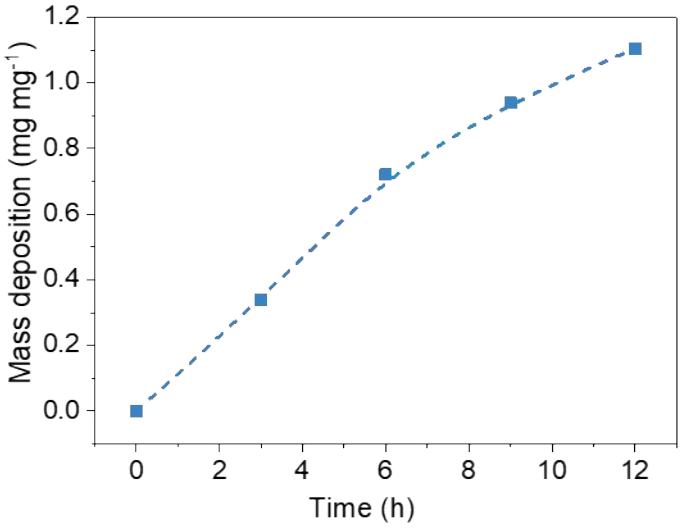

Fig. S15 The weight increase of CMK-3 during the CVD treatment.

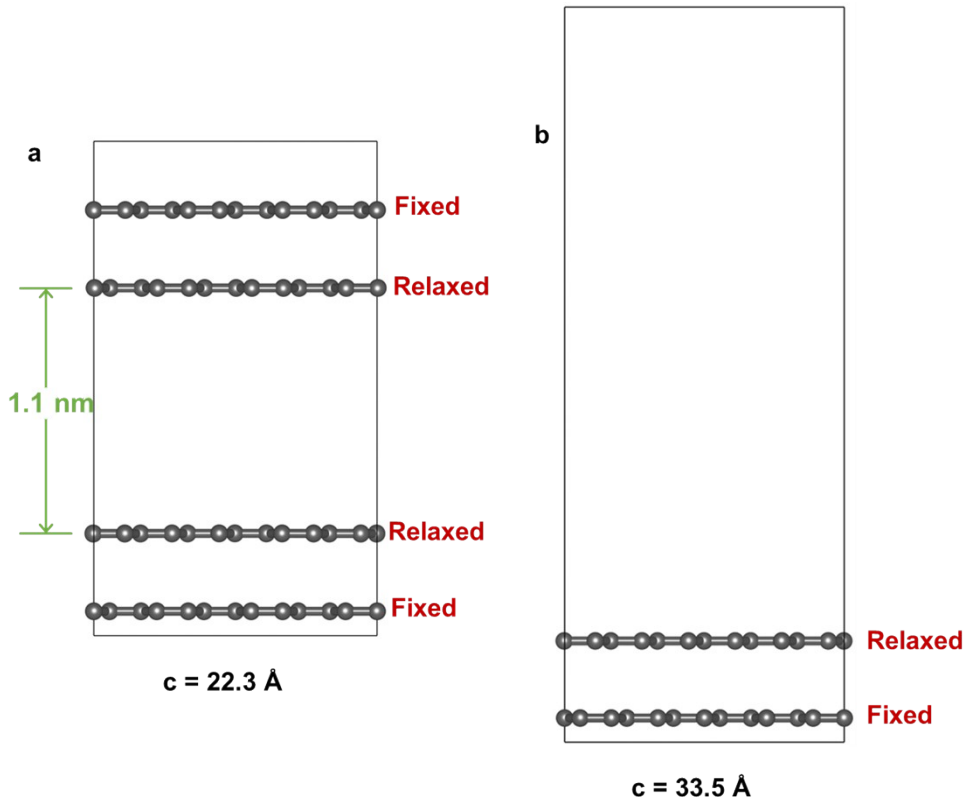

Fig. S16 Slab models for DFT calculations. The (a) space-confined configuration and (b) open configuration.

Table S1. Comparison of the electrochemical performance of different carbon anode materials for SIBs.

Materials	ICE [%]	Reversible capacity [mAh g^{-1}] /current density [mA g^{-1}]	Cycling stability [mAh g^{-1}]	Refs.
Sieving carbons	81	430/50	390 at 50 mA g^{-1} for 100 cycles (93%)	6
Coal-derived HC	82	308.4/30	215.5 at 90 mA g^{-1} for 800 cycles (85.1%)	7
Pitch-derived carbon	80	263/40	184 at 40 mA g^{-1} for 500 cycles (70%)	8
Cherry petals-derived carbon	67	310.2/20	131.5 at 500 mA g^{-1} for 500 cycles (89.8%)	9
Phenol-formaldehyde resin derived carbon	84	410/30	381 at 30 mA g^{-1} for 40 cycles (93%)	10
Waste cork derived HC	81	358/30	312 at 30 mA g^{-1} for 200 cycles (87%)	11
Hard-soft composite carbon	80	282/30	191 at 150 mA g^{-1} for 100 cycles (74%)	12
Pitch derived carbon	72	289/30	270.1 at 30 mA g^{-1} for 100 cycles (93.7%)	13
FC-3h-1300	88.4	435.5/20	413.1 at 50 mA g^{-1} for 100 cycles (99%) 284.0 at 500 mA g^{-1} for 1000 cycles (80%)	This work

Table S2. Comparison of the electrochemical performance of different carbon anode materials for KIBs.

Materials	ICE [%]	Reversible capacity [mAh g^{-1}] /current density [mA g^{-1}]	Cycling stability [mAh g^{-1}]	Refs.
Pitch derived carbon	65	296/27.9	296 at 27.9 mA g^{-1} for 50 cycles (93.2%)	14
Hard-soft composite carbon	67	261/27.9	200 at 279 mA g^{-1} for 200 cycles (93%)	15
Amorphous ordered mesoporous carbon	63.6	307.4/50	146.5 at 1000 mA g^{-1} for 1000 cycles (70%)	16
Hollow nanostructured N-doped carbon	37.92	301.8/100	254 at 100 mA g^{-1} for 100 cycles (84.2%)	17
N/S/O-tridoped HC	31.6	237.8/50	209.6 at 50 mA g^{-1}, 100 cycles, (88.1%)	18
Nitrogen-doped and partially graphitized hard carbons	34.8	269.3/50	137.6 at 500 mA g^{-1} for 1000 cycles (63.2%)	19
Carbon spheres	52.0	239.6/100	140.2 at 2000 mA g^{-1} for 500 cycles (65.8%)	20
MXene-bonded HC film	40	280.6/30	210 at 50 mA g^{-1} for 100 cycles (84%)	21
FC-3h-1300	68.4	376.6/20	322.7 at 50 mA g^{-1} for 150 cycles (96.9%)	This work

Supplementary references

1 J. P. Perdew and Y. Wang, *Phys. Rev. B*, 1992, **45**, 13244-13249.
2 J. P. Perdew, K. Burke and M. Ernzerhof, *Physical Review Letters*, 1996, **77**, 3865-3868.
3 G. Kresse and J. Hafner, *Phys. Rev. B*, 1994, **49**, 14251-14269.
4 G. Kresse and J. Furthmüller, *Physical Review B*, 1996, **54**, 11169-11186.
5 P. E. Blöchl, *Physical Review B*, 1994, **50**, 17953-17979.
6 Q. Li, X. Liu, Y. Tao, J. Huang, J. Zhang, C. Yang, Y. Zhang, S. Zhang, Y. Jia, Q. Lin, Y. Xiang, J. Cheng, W. Lv, F. Kang, Y. Yang and Q.-H. Yang, *Natl. Sci. Rev.*, 2022, **9**, nwac084.
7 K. Wang, F. Sun, H. Wang, D. Wu, Y. Chao, J. Gao and G. Zhao, *Adv. Funct. Mater.*, 2022, **32**, 2203725.
8 Y. Qi, Y. Lu, F. Ding, Q. Zhang, H. Li, X. Huang, L. Chen and Y.-S. Hu, *Angew. Chem. Int. Ed.*, 2019, **58**, 4361.
9 Z. Zhu, F. Liang, Z. Zhou, X. Zeng, D. Wang, P. Dong, J. Zhao, S. Sun, Y. Zhang and X. Li, *J. Mater. Chem. A*, 2018, **6**, 1513-1522.
10 Q. Meng, Y. Lu, F. Ding, Q. Zhang, L. Chen and Y.-S. Hu, *ACS Energy Lett.*, 2019, **4**, 2608-2612.
11 Y. Li, Y. Lu, Q. Meng, A. C. S. Jensen, Q. Zhang, Q. Zhang, Y. Tong, Y. Qi, L. Gu, M.-M. Titirici and Y.-S. Hu, *Adv. Energy Mater.*, 2019, **9**, 1902852.
12 F. Xie, Z. Xu, A. C. S. Jensen, H. Au, Y. Lu, V. Araullo-Peters, A. J. Drew, Y.-S. Hu and M.-M. Titirici, *Adv. Funct. Mater.*, 2019, **29**, 1901072.
13 S. Liu, W. Shao, W. Zhang, T. Zhang, C. Song, M. Yao, H. Huang, X. Jian and F. Hu, *Nano Energy*, 2021, **87**, 106097.
14 Y. Liu, Y.-X. Lu, Y.-S. Xu, Q.-S. Meng, J.-C. Gao, Y.-G. Sun, Y.-S. Hu, B.-B. Chang, C.-T. Liu and A.-M. Cao, *Adv. Mater.*, 2020, **32**, 2000505.
15 Z. Jian, S. Hwang, Z. Li, A. S. Hernandez, X. Wang, Z. Xing, D. Su and X. Ji, *Adv. Funct. Mater.*, 2017, **27**, 1700324.
16 W. Wang, J. Zhou, Z. Wang, L. Zhao, P. Li, Y. Yang, C. Yang, H. Huang and S. Guo, *Adv. Energy Mater.*, 2018, **8**, 1701648.
17 W. Hong, Y. Zhang, L. Yang, Y. Tian, P. Ge, J. Hu, W. Wei, G. Zou, H. Hou and X. Ji, *Nano Energy*, 2019, **65**, 104038.
18 M. Chen, Y. Cao, C. Ma and H. Yang, *Nano Energy*, 2021, **81**, 105640.
19 J. Hu, Y. Xie, M. Yin and Z. Zhang, *J. Energy Chem.*, 2020, **49**, 327-334.
20 X. Han, T. Chen, P. Zhang, Y. Qi, P. Yang, Y. Zhao, M. Shao, J. Wu, J. Weng, S. Li and F. Huo, *Adv. Funct. Mater.*, 2022, **32**, 2109672.
21 N. Sun, Q. Zhu, B. Anasori, P. Zhang, H. Liu, Y. Gogotsi and B. Xu, *Adv. Funct. Mater.*, 2019, **29**, 1906282.